Boundary-Layer Meteorol (2017) 162:503–522
DOI 10.1007/s10546-016-0205-2

RESEARCH ARTICLE

Estimate of Boundary-Layer Depth Over Beijing, China, Using Doppler Lidar Data During SURF-2015

Meng Huang[1,2,3] · Zhiqiu Gao[1] · Shiguang Miao[2] · Fei Chen[4,5] · Margaret A. LeMone[4] · Ju Li[2] · Fei Hu[1] · Linlin Wang[1]

Received: 15 April 2016 / Accepted: 13 September 2016 / Published online: 27 September 2016

Abstract Planetary boundary-layer (PBL) structure was investigated using observations from a Doppler lidar and the 325-m Institute of Atmospheric Physics (IAP) meteorological tower in the centre of Beijing during the summer 2015 Study of Urban-impacts on Rainfall and Fog/haze (SURF-2015) field campaign. Using six fair-weather days of lidar and tower data under clear to cloudy skies, we evaluate the ability of the Doppler lidar to probe the urban boundary-layer structure, and then propose a composite method for estimating the diurnal cycle of the PBL depth using the Doppler lidar. For the convective boundary layer (CBL), a threshold method using vertical velocity variance ($\sigma_w^2 > 0.1\,\mathrm{m^2 s^{-2}}$) is used, since it provides more reliable CBL depths than a conventional maximum wind-shear method. The nocturnal boundary-layer (NBL) depth is defined as the height at which σ_w^2 decreases to 10 % of its near-surface maximum minus a background variance. The PBL depths determined by combining these methods have average values ranging from ≈270 to ≈1500 m for the six days, with the greatest maximum depths associated with clear skies. Release of stored and anthropogenic heat contributes to the maintenance of turbulence until late evening, keeping the NBL near-neutral and deeper at night than would be expected over a natural surface. The NBL typically becomes more shallow with time, but grows in the presence of low-level nocturnal jets. While current results are promising, data over a broader range of conditions are needed to fully develop our PBL-depth algorithms.

Keywords Doppler lidar · Turbulence · Urban boundary layer

✉ Zhiqiu Gao
zgao@mail.iap.ac.cn

1 State Key Laboratory of Atmospheric Boundary Layer Physics and Atmospheric Chemistry, Institute of Atmospheric Physics, Chinese Academy of Sciences, Beijing 100029, China

2 Institute of Urban Meteorology, China Meteorological Administration, Beijing, China

3 University of Chinese Academy of Sciences, Beijing, China

4 National Center for Atmospheric Research, Boulder, CO, USA

5 State Key Laboratory of Severe Weather, Chinese Academy of Meteorological Sciences, China Meteorological Administration, Beijing, China

1 Introduction

Planetary boundary-layer (PBL) structure in urban areas has been an important focus of recent boundary-layer research. Expanding urban areas have replaced the natural land surface with dense buildings, which produce aerodynamically rough and inhomogeneous surfaces. This urbanization can lead to highly complex turbulence structure in the PBL over cities, i.e., within the urban boundary layer (UBL), as well as unique features of the urban climate. The UBL depth is a key variable that describes the boundary-layer structure, and in many applications such as air-pollution prediction and weather forecasting (Beyrich 1997; Miao et al. 2011; Barlage et al. 2016). As for air-quality prediction, small errors in PBL depth can significantly degrade the representation of pollutant transport, dispersion and entrainment in numerical simulations (Zhong et al. 2007; Jiang et al. 2008). This is partly because the PBL depth is an important turbulence length scale used in boundary-layer parametrizations. For instance, both the Yonsei University (YSU) (Hong et al. 2006) and Asymmetric Convective Model, version 2 (ACM2) schemes (Pleim 2007a, b) in the mesoscale Weather Research and Forecasting (WRF) model require estimates of the PBL depth.

Along with the complex structure of the UBL, the practical difficulties in making observations in an urban area also hinder progress towards better understanding of the UBL. It is now almost two hundred years since the first discussion of urban climate based on Luke Howard's direct temperature measurements in London in 1820 (Grimmond 2006). Roth (2000) reviewed a comprehensive series of urban field observations from the early 1950s that were obtained from instruments on balloons, tall TV towers, and even helicopters. These studies show that the UBL and its corresponding urban climate characteristics differ significantly from city to city; thus studies should be conducted according to local conditions.

In China, urban meteorological experiments commenced around 2000. Li and Dou (2014) reviewed field experiments related to the boundary layer, torrential rain, local circulations, turbulent fluxes, and surface energy budgets under urban conditions in Beijing since 2004. Liu et al. (2009) described two UBL observational experiments conducted during the winter of 2006 in Nanjing and their results regarding micrometeorological properties of the urban surface layer. All these efforts mainly focused on the surface layer, which is accessible through instrumentation located on standard micrometeorological towers.

Given that in situ measurements are made from towers with height restrictions, and that frequent radiosonde releases are expensive, remote sensing instruments are preferable for capturing the characteristics of UBL dynamics over long time periods. Many field experiments have demonstrated the feasibility of remote sensing instruments such as radar wind profilers, lidars, and ground-based microwave radiometers to directly and continuously detect the PBL height (Flamant et al. 1997; Westwater et al. 1999; Cohn and Angevine 2000). These experiments occurred mainly over forests, canyons, suburban areas, and over the ocean. However, much more attention has been paid to urban areas in recent years; for example in Hannover (Emeis et al. 2004), Beijing (He et al. 2006), London (Davies et al. 2007), and Houston (Haman et al. 2012). However, appropriate algorithms to derive the PBL depths are required (Emeis et al. 2008).

The Doppler wind lidar is one of the most promising active remote sensors used to obtain wind profiles from the ground up to the lower stratosphere (Chanin et al. 1989; Baumgarten 2010). Satellite-based lidar has the potential to provide wind measurements in regions not sampled by radiosondes or tracking of clouds or other features (Baker et al. 1995; Devara et al. 2015). With improvements in high-energy pulsed lasers, advanced lidars with low-noise detectors and high optical quality telescopes have been evaluated for wind measurements at

ranges up to 10 km, and with low aerosol/cloud droplet concentrations (e.g., Frehlich et al. 1994; Rhodes and Lundquist 2013; Devara et al. 2015). Compared to radiosondes or aircraft, the Doppler lidar has the advantage of superior spatial and temporal resolutions (Devara 1989; Singh and Kavaya 2004).

As part of the 2015 Study of Urban-impacts on Rainfall and Fog/haze (SURF-2015), a high-resolution Doppler lidar and an instrumented 325-m meteorological tower were used to sample the UBL structure. The objectives of the present study are, (1) to determine UBL depths using high-resolution Doppler lidar data for both convective and nocturnal boundary layers, and (2) to investigate the diurnal evolution of urban PBL depths under conditions of differing cloudiness and the nocturnal low-level jet (LLJ). Using the observational dataset obtained from SURF-2015 (described in Sect. 2), we compare the lidar observations with the 325-m tower data in Sect. 3. In Sect. 4 we present methods of determining convective boundary-layer (CBL) and nocturnal boundary-layer (NBL) depths and present sample results. Results based on combining the two methods to produce the entire diurnal cycle for the six days analyzed are discussed in Sect. 5, and we summarize results and suggest future work in Sect. 6.

2 Field Experiment and Data Processing

The Beijing SURF experimental campaign, led by the Institute of Urban Meteorology, China Meteorological Administration (IUM/CMA), is planned for the summer and winter months of each year from 2015 to 2017, focusing on the Beijing–Tianjin–Hebei city cluster. The first summer experiment, which took place from mid-June to early September 2015, was undertaken to investigate the urban PBL structure. Measurements of relevance to this study are based on a high-resolution ground-based Doppler lidar (Leosphere WindCube 100S) and two sets of instruments on the 325-m tower located at the Institute of Atmospheric Physics, Chinese Academy Sciences (IAP/CAS, hereafter IAP) site (see Fig. 1a). The IAP tower is located in the centre of Beijing (Fig. 1b), and is surrounded by commercial and residential buildings; the general building height in the area is 18–19 m, although several very tall buildings (Guanchengyuan Court, 70–90 m high) are located just 150 m south of the 325-m tower (see Fig. 1c). On the IAP tower, there are turbulence instruments (measuring fluxes and variances) at seven levels and meteorological instruments (measuring wind speed, wind direction, relative humidity and air temperature) at 15 levels. The heights are given in Table 1. In addition, vertical profiles are measured using radiosondes launched four times per day at the Nanjiao station, which is located ≈20 km south-east of the IAP tower (Fig. 1b).

2.1 Doppler Lidar Observations

We focus on the Doppler lidar data because of its capability to continuously sample the PBL with high temporal and spatial resolutions. The minimum and maximum ranges of the lidar are 70 m and 3000 m respectively, with 20-m range gates. Although the lidar operated for two months, we report only on the results where the acquired data were complete and of good quality below 2000 m: 5–8 July and 12–13 August. These days were characterized by clear to overcast skies but no precipitation. The limited availability of good quality data was due not only to a weak lidar signal when thicker clouds were present, but also due to power failures during the initial deployment. The lidar was located on grassland about 20 m from the IAP tower (39°58′N, 116°22′E).

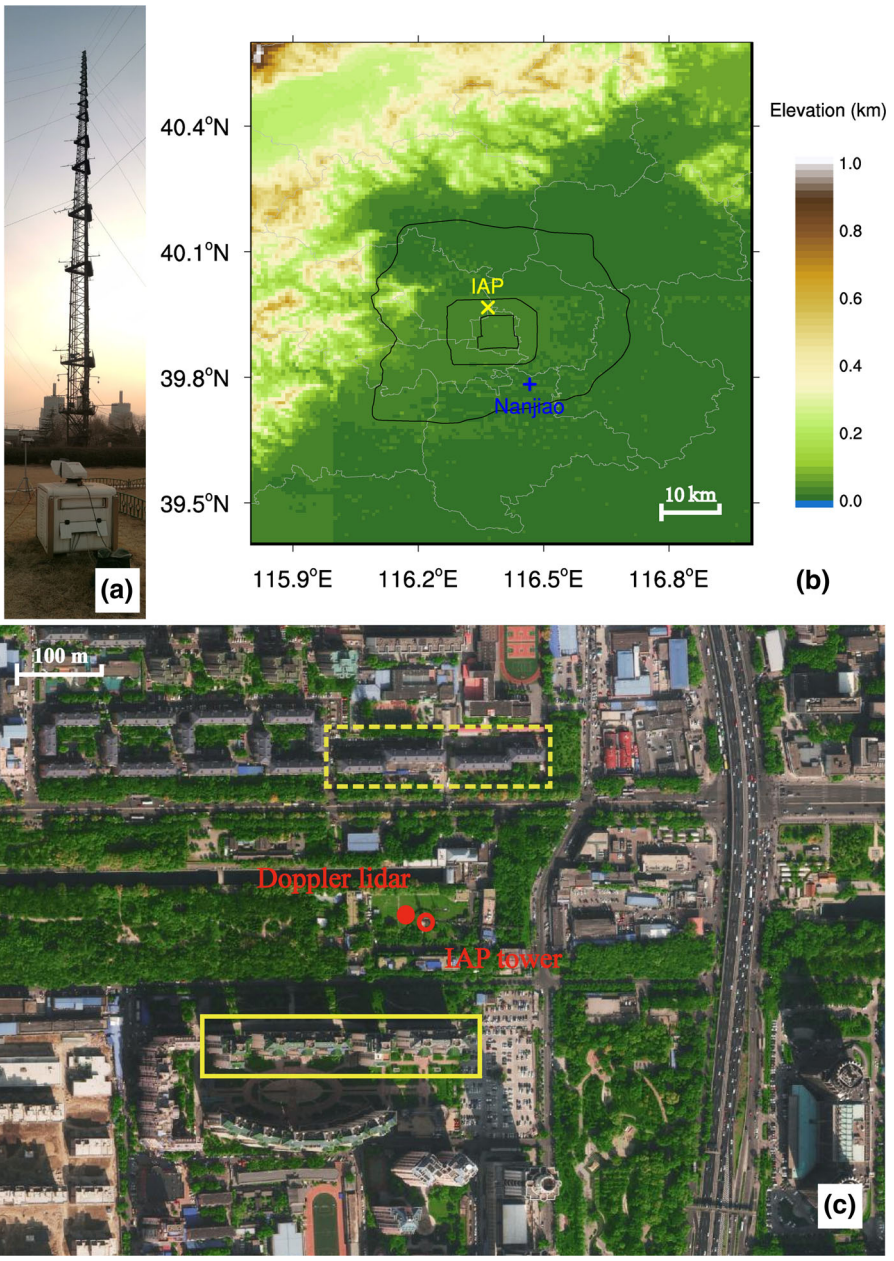

Fig. 1 Site description and observation locations. **a** Photograph of the lidar with the IAP 325-m tower in the background; **b** terrain map of Beijing showing the locations of the IAP 325-m tower (*yellow*×), the Nanjiao sounding site (*blue*+). The three *black rings* represent the second, fourth, and sixth Ring Roads in Beijing, respectively; and **c** IAP tower environment and information on surrounding buildings. The lidar (*red dot*) and the 325-m meteorological tower (*red circle*) are co-located in the IAP yard. Very high buildings in Guanchengyuan Court located south of the IAP tower are indicated by a *solid-line yellow rectangle*. Relatively low buildings in Mudanyuan Court, north of the IAP tower are indicated by a *dashed-line rectangle*

Table 1 Instrument heights on the IAP tower

Height (m)	8	15	32	47	65	80	100	120	140	160	180	200	240	280	320
Meteorological	√	√	√	√	√	√	√	√	√	√	√	√	√	√	√
Turbulence	√	√		√		√			√			√		√	

Table 2 Mean streamline deflection angle and standard deviation at each level resulting from the double coordinate-system rotation

Height (m)	Average (°)	Std (°)
8	−4.96	7.7
16	−3.24	7.6
47	−0.37	5.5
80	−0.69	8.8
140	1.24	7.4
200	1.51	7.8
280	2.15	10.4

A Doppler beam swinging (DBS) scan mode was used to probe the velocity structure of the atmosphere. The beam was directed along five different lines of sight, including four lines-of-sight spaced 90° apart with a fixed elevation angle (75° in this study), and one vertical line-of-sight. Given 4–5 (2–3) s for each 75° (90°) line-of-sight, the total amount of time for an entire DBS scan was ≈20 s. We used only data satisfying a threshold carrier-to-noise ratio (CNR) criterion to reduce the effects of invalid data on profiles derived from the Doppler velocities. Based on examining lidar data for the six days selected, we chose a CNR threshold of ≈ -20 dB in this dataset, and then used the edited data to calculate vertical velocity variance (σ_w^2) and streamwise wind speed and wind direction over 30-min segments.

2.2 Turbulence Measurements (Seven Levels)

The seven sets of turbulence instruments, each located on a cantilever pointing north from the tower, include three-dimensional sonic anemometers (Windmaster Pro, Gill) and open-path gas analyzers (LI-7500A, LI-COR) to measure wind velocity, air temperature, water vapour and CO_2 concentrations at a frequency of 10 Hz. Available datasets from this tower and calculated turbulent fluxes have been documented elsewhere (e.g., Hu et al. 1999; Al-Jiboori 2008; Miao et al. 2012). We analyzed data in 30-min segments to capture most scales of turbulence, using the common block-averaging method to extract turbulent fluctuations. Data quality control included eliminating spikes and points outside absolute limits in each period. Velocity variances were calculated using a natural wind coordinate system with double rotation (Wilczak et al. 2001). For the present dataset, the mean vertical streamline deflection (Ψ) at each level is given in Table 2, and we note that the downward streamline deflection below 80 m is likely explained by the cavity effect [Fig. 8.1 in Oke (2002)] induced by the tall buildings south (upstream) of the tower. Positive pitches at heights above 140 m suggest deflection around the individual buildings and the tower envelope. Periods with extreme vertical pitch (beyond 2.5 standard deviations) are rejected from our analysis.

2.3 Mean Wind Observations (15 levels)

At each of 15 levels, cup anemometers (MetOne 010C) and wind vanes (MetOne 020C) sampled the wind speed and direction at 0.05 Hz, at a resolution of 0.1 m s^{-1} and 0.1°. To reduce the interference effects from the tower, the anemometers were installed at the ends of two sets of horizontal steel cantilevers, one extending toward the north-west (prevailing wind direction during the winter) and one extending toward the south-east (prevailing wind direction during the summer), at each measurement level. Wind vanes were installed only on the south-east-pointing cantilever. We used the 30-min average wind speeds and directions calculated from the instruments to the south-east of the tower because the wind direction was from the south during the study period.

2.4 Radiosondes

GPS radiosondes were released daily from the Nanjiao station at 0115, 0715, 1315, and 1915 LST (= UTC+8, solar noon at 1200 LST) during the summer phase of SURF-2015 to sample wind velocity, temperature, pressure and relative humidity (at 0115 LST only wind data were logged). The Nanjiao station, classified as "urban" based on the MODIS land-use classifications, is located in the southern suburbs of Beijing, about 20 km from the IAP tower. We used the potential temperature (θ) profile at 1315 LST to represent the typical CBL structure. Several slightly different θ-based methods for determining PBL depths were described in LeMone et al. (2013). Given the distance between IAP and Nanjiao, the PBL depths from radiosonde soundings are not expected to correspond exactly to those from the lidar data.

3 Evaluation of Doppler Lidar Observations

In order to evaluate the lidar's performance, profiles of the streamwise wind component (U) and the vertical velocity standard deviation (σ_w) calculated from the DBS scan data were compared to those derived from the meteorological and turbulence measurements from the IAP tower, respectively. Both the time variation of downward shortwave radiation (not shown) and the ratio (S_T) of daily total downward shortwave radiation at 140 m to that reaching the top of atmosphere were used to identify fair weather, following Miao et al. (2012). If $S_T \geq 0.8$, the weather was considered fair, with clear skies for smoothly varying downward shortwave radiation, and partly cloudy skies if the downward shortwave radiation varied. If $S_T < 0.8$, the day was considered overcast. According to this definition, fair-weather days were identified as 5 July (partly cloudy), 7 July (clear) and 12 August (clear); the overcast days were 6 July, 8 July and 13 August.

Sample wind profiles from tower and lidar data on 6 July are shown in Fig. 2, and shows an improved lidar-tower agreement at night (0200 LST) than during the day (1400 LST). A likely reason is that cup anemometers tend to measure a higher wind speed under unstable conditions (Kaganov and Yaglom 1976). To quantify the measurement bias between the lidar and tower measurements, we calculated height-averaged biases, absolute biases, and root-mean-square differences (*RMSE*), using the 30-min averaged lidar profiles. Since the lidar observation heights do not necessarily match those from the tower, we linearly interpolated lidar wind speeds to the tower measurement heights. Table 3 lists the height-averaged statistics for 0200 and 1400 LST; importantly, the lidar data show a reasonably good agreement with the tower data, indicating the lidar's potential for indicating PBL evolution in an urban environment.

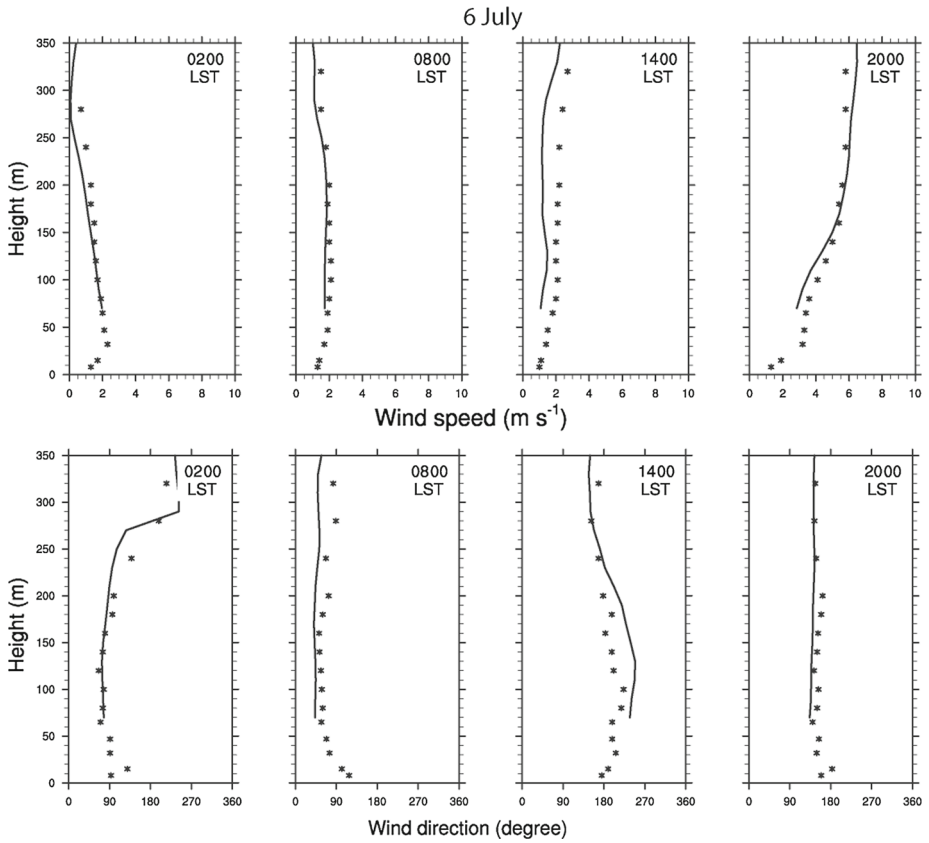

Fig. 2 30-min averaged vertical profiles of streamwise wind speed (*top*) and wind direction (*bottom*) calculated from the DBS scans at 0200, 0800, 1400 and 2000 LST on 6 July. Corresponding variables obtained from the IAP tower are indicated by *asterisk* symbols

Table 3 The height-averaged mean bias (lidar minus tower), mean absolute bias, and root-mean-square difference of wind speed between lidar and tower for day (1400 LST), night (0200 LST), and for all hours during the study period

Hours (LST)	Mean bias (m s^{-1})	Mean absolute bias (m s^{-1})	*RMSE* (m s^{-1})
1400	−0.51	0.64	0.72
0200	−0.17	0.20	0.26
All	−0.18	0.31	0.42

Figure 3 shows a comparison of the 30-min vertical velocity standard deviation between lidar and tower measurements at four heights, given by

$$\sigma_w = \sqrt{\left(\frac{1}{N-1}\right)\sum_{i=1}^{N}(w_i - \bar{w})}, \quad (1)$$

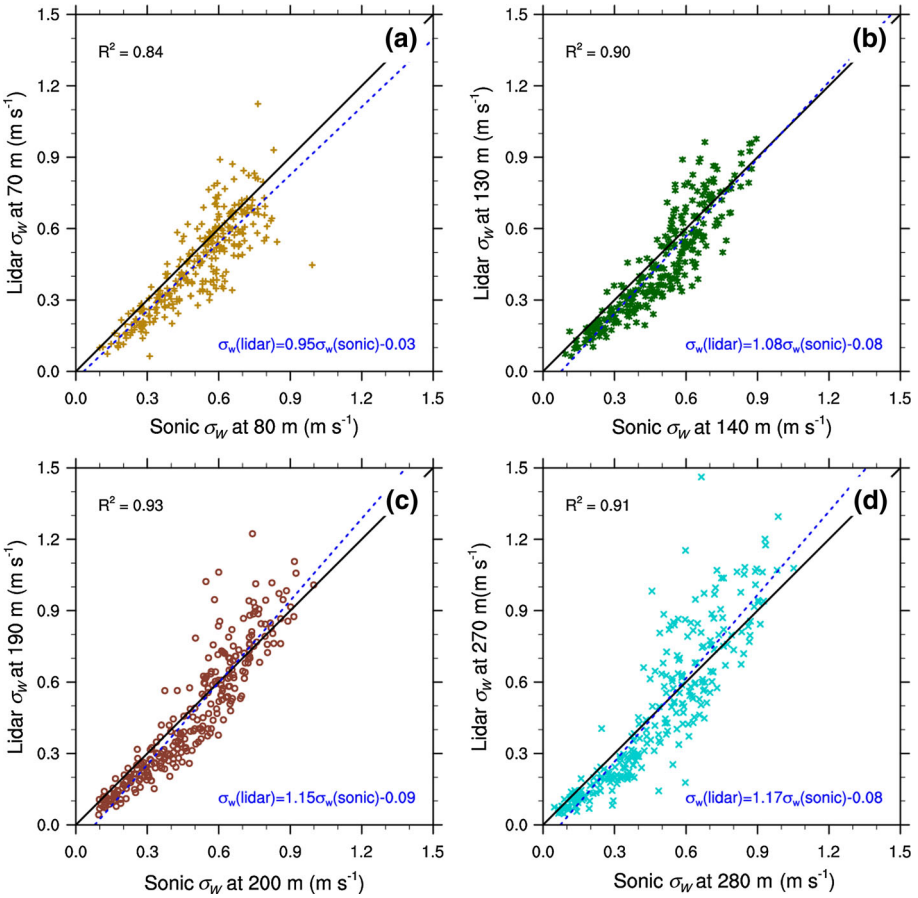

Fig. 3 Scatter plot of σ_w calculated from lidar data compared to 30-min sonic-anemometers averages at four different heights: **a** lidar at 70 m versus tower level of 80 m; **b** lidar at 130 m versus tower level of 140 m; **c** lidar at 190 m versus tower level of 200 m; and **d** lidar at 270 m versus tower level of 280 m. The *black solid lines* indicate the 1:1 lines, while the *blue dashed lines* are least-squares best-fit lines

where N is the number of samples, w_i denotes the i^{th} vertical velocity, and $\bar{w}$ is mean vertical wind speed. Note that, for sonic anemometer measurements, $\bar{w} = 0$ due to the double-rotation of the coordinate system. There are three deductions that can be made from the figure. First, the wind speeds at levels above 140 m ($R^2 = 0.90$, 0.93, and 0.91 at heights of 140, 200, and 280 m) are more strongly correlated than those at 80 m ($R^2 = 0.84$). Second, the slopes of all four best-fit lines are close to 1; however, the lidar underestimates σ_w at 80 m (slope = 0.95), and overestimates σ_w above 140 m (slopes > 1). Based on the aerodynamic and thermodynamic scaling properties for bluff buildings in urban area, Roth (2000) defined four sub-layers in the urban PBL (moving upwords from the surface): the urban canopy layer, the roughness sublayer, the constant-flux layer and the mixed layer. Miao et al. (2012) examined the characteristics of friction velocity using IAP tower data at heights of 47, 140, and 280 m, and concluded that the level of 47 m is within the roughness sublayer and that at 140 m is within the constant-flux layer. In this study, the relatively lower correlation coefficient at 80 m may be due to the fact that the 80-m level is within the roughness sublayer, where

the dominant controls on turbulence are high roughness elements (i.e., buildings) and the turbulence field is often horizontally heterogeneous.

In addition, it is noteworthy that the lidar underestimated σ_w at all four heights for the sonic measured $\sigma_w < 0.5$ m s^{-1} and overestimated σ_w for the sonic measured $\sigma_w > 0.6$ m s^{-1}. Since the lidar sampling frequency (≈ 0.05 Hz) is less than that of the tower sonic anemometers (10 Hz), the lider does not capture high-frequency turbulence. Thus, one would expect the lidar to underestimate σ_w. The reason for the overestimates for the larger values of sonic measured σ_w is unclear and requires further investigation.

4 Determination of PBL Depths

4.1 Determination of the CBL Depths

4.1.1 Defining CBL Depth Using the Threshold Method

The vertical-velocity variance (σ_w^2) from the lidar was used to determine the PBL depth, for heights above the lidar's minimum range of 70 m. Previous investigators have found that defining the PBL as that layer for which σ_w^2 exceeds a given threshold is reliable, although the precise value of that threshold appears to be site-dependent. For example, Tucker et al. (2009) empirically determined the optimum threshold for the dataset obtained from TexAQS-2006 to be 0.04 m^2 s^{-2}, though such a low value may have been due to the weak turbulence in air of marine origin; other threshold values have been larger. Pearson et al. (2010) combined $\sigma_w^2 > 0.3$ m^2 s^{-2} and the first minimum found in the backscatter gradient for determining the PBL depth for a highly convective tropical boundary layer over a tropical rain forest. Barlow et al. (2011) defined the mixing height as the height up to which $\sigma_w^2 > 0.1$ m^2 s^{-2} for observations over central London, UK.

Here, we selected Barlow's σ_w^2 threshold of 0.1 m^2 s^{-2}, since our data are also for an urban environment; an example of employing this threshold is shown in Fig. 4. The PBL started to grow after sunrise (0452 LST), and deepened to a maximum value in mid-afternoon; the whole layer remained convectively unstable and well-mixed during the daytime hours. The fully developed CBL reached a depth of ≈1850 m between 1400 and 1800 LST, and

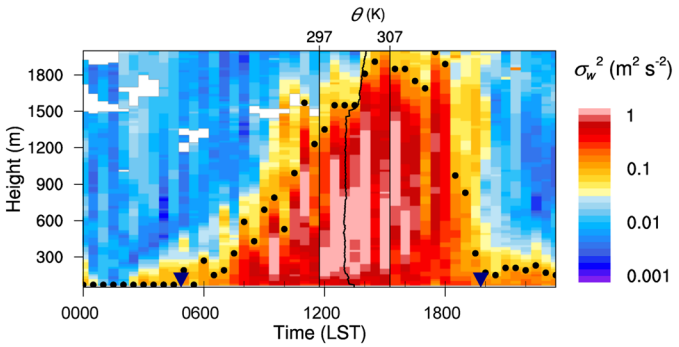

Fig. 4 For 6 July, 30-min averaged vertical velocity variance, σ_w^2 (m^2 s^{-2}), calculated from the DBS data. PBL depths based on the threshold method are indicated by *black dots*. Also displayed is the potential temperature (θ) profile, based on the 1315 LST Nanjiao sounding. The *vertical lines* labeled 297 K and 307 K define the scale for the sounding profile. Sunrise and sunset times are marked by *triangles*

after 1800 LST, roughly two hours before sunset, the thermals disappeared, the turbulence weakened, and the CBL depth as defined here decreased rapidly. Note that the PBL depths derived from σ_w^2 are reasonably consistent with the Nanjiao 1315 LST sounding (Fig. 4), even though Nanjiao is 20 km distant and likely has a different upstream fetch. Thus the CBL depths estimated using the 0.1 m^2 s^{-2} threshold method appear reasonable.

4.1.2 Validation of Derived CBL Depths Using a Wind-Shear Method

Since the threshold value was empirically determined, it is important to assess its robustness as a threshold for estimating PBL depth. Following the same approach as in Barlow et al. (2011), we introduced a 10 % perturbation to the threshold criterion. We found that 81 % of the estimated PBL depths were within one gate (20 m) of the original estimates, while 10 % differed by two or three gates, and 10 % differed by four gates or more.

In a second test, we compared PBL depths using a wind-shear method, based on the idealized CBL, to our threshold-based CBL depths. As illustrated in Stull (1988), wind speed and direction, potential temperature, and mixing ratio are nearly uniform through a "mixed layer" that extends through most of the idealized CBL. Beneath, the mean horizontal wind speed decreases to zero logarithmically in a shallow surface layer. Above the mixed layer, the wind speed changes from its mixed-layer value to the free atmosphere value above a transition layer, which corresponds closely to the inversion layer that marks the top of the CBL. Thus, the height above the mixed layer at which a sharp change in the wind profile occurs is a good candidate for an independent estimate of CBL depth. Here, we define the PBL top as the point at which the vertical shear of the horizontal wind reaches a maximum. The vertical wind shear ($\Delta \boldsymbol{V}/\Delta z$) for a layer of thickness Δz was calculated from

$$\frac{\Delta \boldsymbol{V}}{\Delta z} = \frac{\sqrt{(u_t - u_b)^2 + (v_t - v_b)^2}}{(z_t - z_b)}, \tag{2}$$

where u is the zonal component of the wind speed, v is the meridional component, and z is the observation height. The subscripts b and t denote the bottom and top of the layer.

Figure 5 shows the lidar daytime wind-speed profiles for 5 and 8 July together with CBL depths estimated using the threshold method. The weather was fair and flow weak on 5 July. Threshold-based CBL depths show good agreement with h_{shear}, except for 1200 LST, particularly if one recognizes that the wind-shear maximum could identify the centre of the transition layer, while the slightly smaller σ_w^2 threshold-based depth could identify the top of the well-mixed layer (and base of the transition layer). At 1200 LST, the elevated maximum-shear layer could be associated with the wind change resulting from the radiosonde entering or leaving a cumulus cloud. Since cumulus clouds commonly occur atop the CBL over land (Angevine 2005), we conclude that the derived CBL depth from the threshold method is slightly more reliable than that using the maximum wind-shear method on this day.

In contrast, 8 July was predominantly overcast. The decrease in wind speed around 1500 m at 1000 and 1200 LST, associated with the top of the cloud layer, is more pronounced than that at 1200 LST on 5 July. At 1000 LST, h_{shear} is much higher than the depth of the subjectively determined transition layer, which appears to be centred around 800 m as well as the threshold-based (mixed-layer) top at around 700 m. The shear layer at around 1200–1500 m was likely not connected to the CBL, since it appeared to be at the top of a stratus layer, based on radiosonde winds, temperatures, and dew points earlier in the morning when the CBL was much shallower. At noon, the subjective transition layer appears to correspond to the wind speed increase starting at the threshold-based height. In the mid-afternoon (1400–1600 LST), the shear-based CBL depths are, like those for 5 July, just above those based

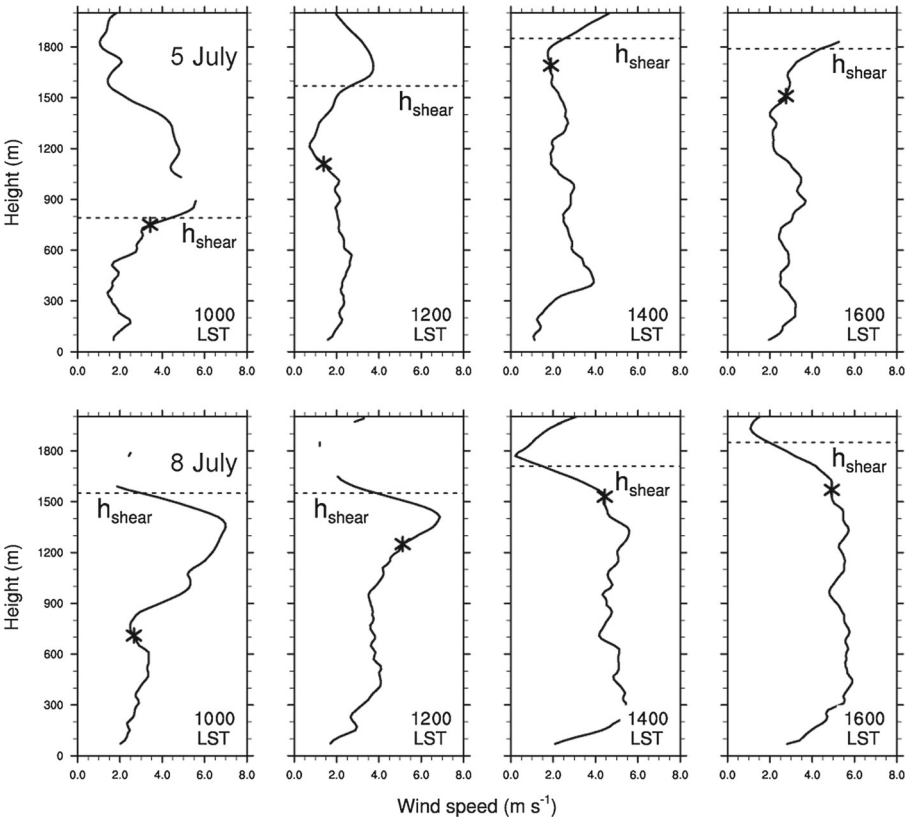

Fig. 5 Daytime 30-min average wind-speed profiles calculated from the DBS data for the CBL at 1000, 1200, 1400 and 1600 LST on 5 July (fair-weather day, *top*) and 8 July (overcast day, *bottom*). Heights (h_{shear}) where maximum wind-vector gradients occur are denoted by *dashed lines*; *asterisks* indicate CBL depths based on the threshold method

on the σ_w^2 threshold, suggesting the CBL tops lie within the transition layer. Consequently, using the vertical gradient of wind speed alone to detect CBL depths can be misleading.

4.2 Determination of the NBL Depths using the Fractional Method

While the CBL has a well-defined mixed-layer top, the NBL often has a complex structure that varies with time and hence it is more difficult to determine its depth. In the foregoing sections, we have discussed and validated the threshold method when applied to the CBL. We now focus our attention to the challenging problem of estimating NBL depths.

4.2.1 Limitations of Threshold Method

Referring back to Fig. 4, the threshold method failed to determine the PBL depths for late night (0000–0500 LST), one likely explanation being that the NBL was too shallow, falling below the first lidar range gate (70 m). In order to test this hypothesis, we checked the magnitude of σ_w^2 below 50 m using the tower turbulence measurements (Fig. 6), noting that

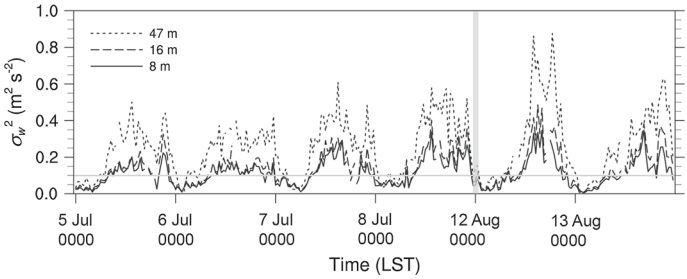

Fig. 6 Time series of 30-min averaged vertical velocity variance, σ_w^2 (m^2 s^{-2}), obtained from the tower IAP tower 10-Hz data at heights of 8, 16 and 47 m for all six days. The threshold value applied in this study (0.1 m^2 s^{-2}) is marked by a *horizontal grey line*. A *thick vertical grey line* separates the two time periods

$\sigma_w^2 < 0.1$ m^2 s^{-2} during all six nights. Given that the NBL often has $\sigma_w^2 < 0.1$ m^2 s^{-2} (e.g., LeMone et al. (2014)), this criterion cannot be used to define its depth.

Also, even when $\sigma_w^2 > 0.1$ m^2 s^{-2}, the threshold-derived NBL depth for early evening (2000–2400 LST) can be very sensitive to the threshold value used. Although there was intense enough turbulence meeting the criterion of $\sigma_w^2 > 0.1$ m^2 s^{-2} and a large σ_w^2 gradient for the NBL between 2000 and 2400 LST on 6 July (Fig. 4), the σ_w^2 gradient is less than that for cases on the other nights (not shown), increasing the sensitivity to the threshold selected. This motivates us to explore other techniques for estimating NBL depths.

4.2.2 NBL Features and Classification

Numerous methods for determining the NBL depth such as the use of potential temperature, humidity, wind speed, and bulk Richardson number based on profiles or radiosonde soundings have been discussed previously [e.g., LeMone et al. (2014)]. Notably, such profiles do not always reflect the turbulence properties in the NBL, therefore using high-frequency turbulence measurements to determine the NBL depth is highly desirable. When turbulence data are available, reliable NBL depth estimates may be based on the height at which a second-moment variable such as the buoyancy flux (Caughey et al. 1979), the vertical component of the horizontal momentum along the surface wind direction (Kosovic and Curry 2000), vertical velocity variance (Vickers and Mahrt 2004), or turbulent kinetic energy (TKE) (Lenschow et al. 1988) decreases to a specific fraction of its surface or near-surface maximum. Fortunately, such parameters tend to be internally consistent, at least for the weakly stable NBL (LeMone et al. 2014). The other thing to note is relatively large measurement errors may be introduced under very stable conditions (Sathe et al. 2011), and so it is imperative to understand and correctly categorize the NBL regimes before adopting a method for estimating the NBL depth.

The NBL varies from being continuously turbulent and fully coupled to the surface regionally to being weak and intermittently coupled with the surface (LeMone et al. 2003). By exploring the dependence of local turbulence on mean wind speed in the stable boundary layer over a grassland site from the Cooperative Atmosphere-Surface Exchange Study in 1999 (CASES-99), Sun et al. (2012) identified three turbulence regimes in the context of the NBL: regime 1 (very stable) with weak turbulence driven by local gradients; regime 2 (near-neutral) with strong turbulence driven by bulk shear (defined as the mean wind speed divided by the observation height); and regime 3 (weakly stable) with moderate turbulence transported from above.

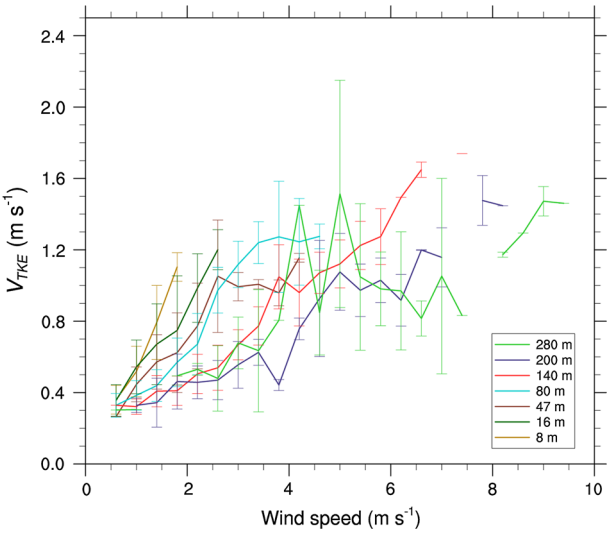

Fig. 7 For the six case-study days, the nocturnal relationship between bin-averaged turbulent intensity V_{TKE} (m s^{-1}) and wind speed (m s^{-1}) for the IAP tower, for points within the NBL. The data are 30-min averages of the 10-Hz turbulence measurements at each level, from 2030 to 0400 LST. The standard deviation of V_{TKE} for each wind-speed bin is marked by a *vertical line*

To identify the turbulence regimes for SURF-2015, we applied the analysis method of Sun et al. (2012) to our dataset throughout the night (2030–0400 LST) during the study period, and the results are shown in Fig. 7. In the figure the TKE $V_{\mathrm{TKE}}^2 = \frac{1}{2}\left(\sigma_u^2 + \sigma_v^2 + \sigma_w^2\right)$ is used to represent the turbulent intensity. For levels $\leq$80 m, V_{TKE} increases rapidly and linearly with wind speed, which corresponds to the near-neutral regime 2. The slopes for tower levels above 140 m but within the NBL are all greater than 0.17, which is closer to the slope for regime 2 (0.25) than to regime 1 (0.03). Thus we classify the regime above 140 m as regime 2. That is, the very stable regime 1 where V_{TKE} is small and increases only slightly with wind speed, does not appear for the days analyzed here.

The absence of the very stable NBL regime is further confirmed by the positive (albeit small) sensible heat fluxes (i.e., upward transfer of sensible heating) in Fig. 8. Such small upward sensible heat fluxes persisted between 2000 and 2400 LST because of anthropogenic heating and the release of heat stored in urban structures (building, roads, etc.). The resulting heat fluxes help sustain turbulence during much of the night. Combined with rough surface elements, the fluxes ensure that atmospheric stratification over cities is usually slightly unstable or near-neutral even on clear nights. Only a few urban measurements have been made under stable conditions (e.g., Roth 2000).

4.2.3 Defining the NBL Depth Using Fractional σ_w^2

Now that we have established that all days analyzed refer to a near-neutral NBL regime, we use a slightly altered version of the LeMone et al. (2014) method, which defines the NBL top as the height at which TKE decreases to a specific fraction of its near-surface maximum after subtracting out a "background" (free atmosphere) value. Here, we substitute vertical

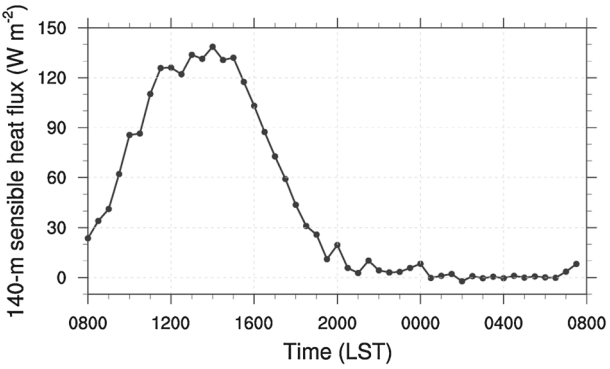

Fig. 8 Sensible heat fluxes (W m^{-2}) measured at 140 m (within the constant-flux layer) on the IAP tower. The results are the average of 41 fair-weather days in July and August 2015

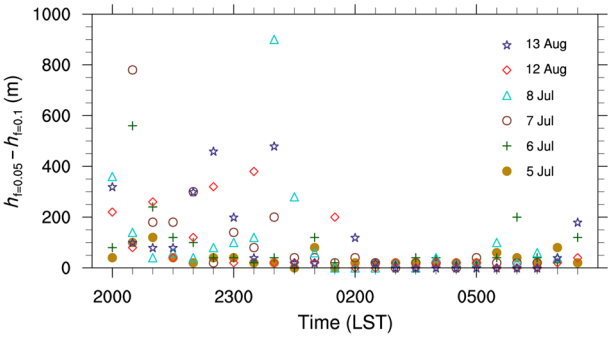

Fig. 9 Difference between NBL depths using $f = 0.05$ and $f = 0.1$ in Eq. 4

velocity variance, σ_w^2, for TKE, following Vickers and Mahrt (2004). Thus, the vertical velocity variance at the top of NBL ($\sigma_{w_\mathrm{h}}^2$) satisfies

$$\sigma_{w_\mathrm{h}}^2 = f\left(\sigma_{w_\mathrm{max}}^2 - \sigma_{w_\mathrm{b}}^2\right) + \sigma_{w_\mathrm{b}}^2, \tag{3}$$

where $\sigma_{w_\mathrm{max}}^2$ is the near-surface maximum value, the fraction $f = 0.05$ or 0.10, and the background value $\sigma_{wb}^2 = 0.01$ m^2 s^{-2}, based on the nocturnal σ_w^2 average above 1000 m.

Differences in NBL depths based on the two values of f are shown in Fig. 9. The NBL depths are close between 0000 and 0700 LST, but differ significantly between about 2000 and 2400 LST; sunset is at around 1945 LST in July and 1915 LST in August. For these cases, the NBL depths using $f = 0.1$ and $f = 0.05$ have been compared to subjective estimates of NBL depths based on the lidar wind-speed profiles (e.g., Banta et al. 2003; Pichugina and Banta 2010). Comparing results from all profiles during the study period, the value of $f = 0.1$ produced a better agreement with the subjectively determined NBL depths; therefore we selected $f = 0.1$ for this dataset.

So far, we have explained the rationale for using two methods (i.e., the threshold and the fractional method) for determining CBL and NBL depths. We now combine them to determine PBL depth over the entire diurnal cycle in the next section.

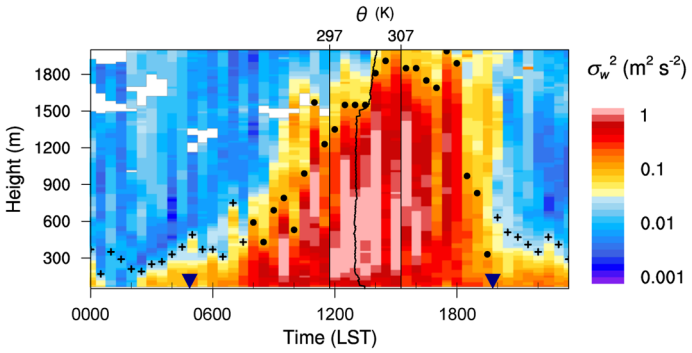

Fig. 10 Same as Fig. 4 for 6 July, except that the fractional method is used for the NBL estimate, denoted with a *plus* (+)

5 Combined PBL Depths Estimated from Doppler Lidar

The threshold method does not work well at night, while the fractional method fails to determine the PBL depth for most of the daytime. Interestingly, during the transition periods (0700–0800 and 1900–2000 LST), these two methods yield similar values of the PBL depth. Thus we can use these time periods to switch between the threshold method and the fractional method, and an example of objectively determined PBL depths by combining these two methods is shown in Fig. 10. We see that the combined method appears to represent PBL evolution reasonably well, suggesting the depths so determined provide a basis for comparisons with those from other urban and rural areas.

Figure 11 shows PBL depths based on the threshold method for the CBL and the fractional method for the NBL, for the six days investigated here. On average, the PBL starts to grow significantly about 3 h after sunrise. Although downwelling solar radiation reaches its maximum value at solar noon (≈1200 LST), the PBL depth reaches its maximum at ≈1400 LST. As illustrated in Figs. 4 and 10, the CBL remains convective, with strong plumes rising from the surface, until about two hours before sunset. After about 2200 LST, the NBL depth decreases slowly throughout the night, reaching its minimum just before sunrise. Haman et al. (2012) also observed a continuous decline of NBL depth over a near-coastal urban environment, mainly due to the increasing stability caused by radiative cooling and the reduction in anthropogenic activities (e.g., traffic and air-conditioning). However this behaviour is not universal; LeMone et al. (2014) found during CASES-97 that the NBL depth grew slightly during three moderately windy fair-weather nights over a rural area covered mostly with grass and crops. Largely due to the relatively high wind speeds on these three nights, the deep NBL and continuous coupling of the atmosphere to the surface are due to shear production of turbulence.

In Fig. 11, the averaged combined PBL depths derived from σ_w^2 vary diurnally from ≈270 to ≈1500 m, though we also investigated the diurnal evolution of PBL depth for the fair-weather and overcast days separately (dashed lines). The largest differences are for the 4-h period centred at sunset. Stronger solar radiation for the fair-weather cases (averaged daytime net radiation: 400W m^{-2}, calculated from Table 4) provides a basis for generating more vigorous thermals, and that prevent the PBL from collapsing sooner, when compared to the cloudy cases (averaged daytime net radiation: 337 W m^{-2}).

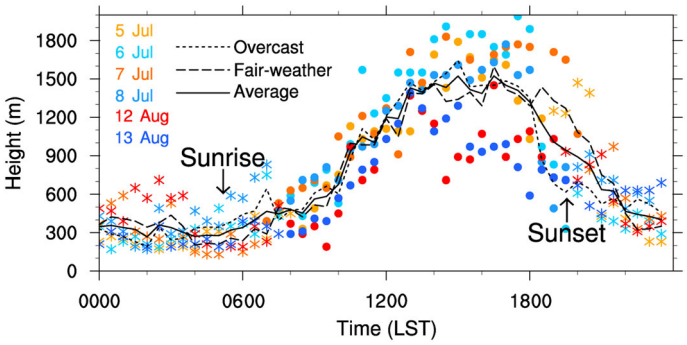

Fig. 11 Time series of PBL depth based on the threshold method for the CBL (*dots*) and the fractional method for NBL (*asterisks*). The *solid*, *long dashed*, and *short dashed lines* represent the average diurnal cycles for all periods, fair-weather days and overcast days, respectively

Table 4 Daytime and 24-h mean energy fluxes for each day during the study period, for net radiation (Q_*), sensible heat (Q_h), and latent heat (Q_e) at a height of 140 m

Date	Daytime (0700–1830 LST)			Daily		
	Q_* (W m^{-2})	Q_h (W m^{-2})	Q_e (W m^{-2})	Q_* (W m^{-2})	Q_h (W m^{-2})	Q_e (W m^{-2})
5 July	402	137	85	176	69	55
6 July	351	102	76	150	51	42
7 July	398	130	101	172	65	58
8 July	330	124	71	139	72	42
12 August	398	59	139	170	30	76
13 August	331	75	64	139	36	37

However, there are other significant day-to-day variations shown in Fig. 11, notably: (1) a shallower CBL depth for the August days than for the July days, and (2) an increasing NBL depth from 2100 to 2400 LST on 13 August and from 0000 to 0300 LST on 12 August. The shallower CBL depths in August mainly result from the smaller surface sensible heat fluxes (Table 4). On the fair-weather day, 12 August, the large fraction of available energy converted into latent heat flux (139 W m^{-2}) is at the expense of sensible heat flux; on the cloudy day, 13 August, the net radiation reduction due to clouds leads to smaller sensible heat fluxes.

The two cases for which the NBL depth increases appear to be associated with shear-generated turbulence in the presence of a LLJ. To show this, we test for LLJ occurrence using the objective criterion developed by Andreas et al. (2000). That is, if a local maximum in the wind-speed profile is 2 m s^{-1} greater than the wind speeds 260 m above and below, it is considered an LLJ. Using 30-min averaged wind-speed profiles from the Doppler lidar, we determined the statistical characteristics of the LLJ at night (2000-0400 LST) during the study period (Table 5). The frequent and strong jets between 0000 and 0400 LST on 12 August (89 %, 8 m s^{-1}) and between 2000 and 2300 LST on 13 August (75 %, 13 m s^{-1}) are entirely consistent with the NBL growth at these times, and can be considered contributing factors to the turbulence development. Wind profiles for the two nights are shown in Fig. 12.

Table 5 For the low-level jet at night (2000-0400 LST), average occurrence frequency, wind-speed maximum (U_x), and height (Z_x) during the study period, based on the 30-min lidar wind-speed profiles

Local time	Frequency (%)		U_x (m s^{-1})		Z_x (m)	
	0000–0400	2000–2330	0000–0400	2000–2330	0000–0400	2000–2330
July 5	0	0	/	/	/	/
July 6	0	25	/	8.4	/	400
July 7	0	0	/	/	/	/
July 8	0	25	/	8.8	/	510
August 12	89	38	7.8	7.4	460	470
August 13	44	75	4.1	13	700	563

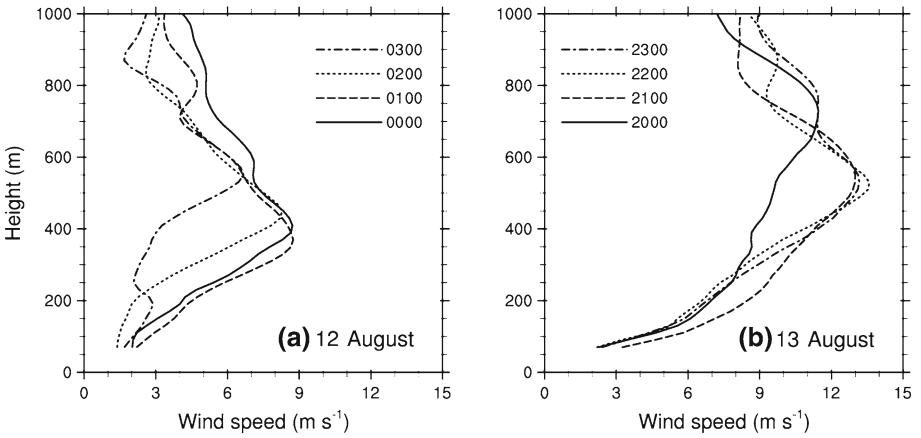

Fig. 12 Doppler lidar 30-min average wind-speed profiles for (**a**) 0000-0300 LST 12 August and (**b**) 2000-2300 LST 13 August. The half-hour profiles are omitted for clarity

6 Summary

During the SURF-2015 summer experiment, a high-resolution Doppler lidar and the collocated IAP long-term 325-m meteorological tower, were deployed in the centre of Beijing with the aim of determining boundary-layer depth and its diurnal evolution. A composite method for estimating PBL depth using a Doppler lidar dataset was presented. Two sets of multilevel observation systems on the tower were used to comprehensively sample the details of boundary-layer structure below 325 m. In combination with the radiosondes released at the Nanjiao Station ≈20 km to the south-east, a six-day dataset allowed us to better describe the local atmospheric environment of Beijing under convective and nocturnal conditions.

The 325-m IAP tower data were used to complement the lidar data because of the lidar's dead zone below 70 m. Based on several calculated variables (e.g., streamline pitch and tower-lidar correlation coefficients) from these two datasets, we can identify the roughness sublayer and constant-flux layer from the data; 30-min average profiles of horizontal wind speed obtained from the lidar were compared with those from sensors at 15 levels on the IAP tower. Additionally, we compared the standard deviations of vertical velocity calculated from the lidar to those from the seven-level sonic anemometer system on the tower. The good

agreement implies that the lidar is able to capture microscale turbulence characteristics and has the potential to determine turbulence-based PBL depths.

Profiles of vertical velocity variance σ_w^2 acquired from the Doppler lidar were used to estimate PBL depth. While the CBL has strong turbulence and sharp gradients at the top of PBL, the observed NBL is usually weakly unstable to near-neutral. Because of the differing turbulence characteristics of the daytime and nocturnal boundary layers, we determined PBL depth and its diurnal evolution by applying the 0.1 m^2 s^{-2} threshold for σ_w^2 of Barlow et al. (2011) for the CBL and a 10 % fractional method for the NBL, following LeMone et al. (2014), which identifies the depth from the height at which σ_w^2 has decreased to 10 % of its near-surface maximum value, minus its background (free-atmosphere) value. The variance-derived CBL depths were realistic for all days analyzed here, and were generally consistent with CBL depths from the Nanjiao radiosonde soundings, even though the two sites are ≈20 km apart. A method that identified the CBL top with the maximum vertical shear in the lidar wind profile succeeded when the maximum wind shear corresponded to the middle of the transition layer, but failed when the method identified a shear layer above the PBL. Note that while the fractional method worked well for the data shown here, it may not be applicable when the boundary layer is strongly stable.

The derived heights for the study period were combined to produce a single time series aimed at investigating the characteristics of diurnal PBL variability. During the day, the partition of sensible and latent heat and the amount of cloudiness affected the urban surface energy fluxes and CBL growth, as expected. During most nights, the NBL depth decreased slightly with time, although it deepened in the presence of enhanced LLJ turbulence production.

This study was an attempt to utilize a high-resolution Doppler lidar to estimate PBL depths under a wide range of stability conditions in Beijing for the first time. In general, the urban boundary-layer structure and evolution observed for our limited number of cases were similar to what has been observed previously. However, the nocturnal boundary layer remained near-neutral: the widely documented "upside-down boundary layer", "downward mixing regime" (e.g., Banta et al. 2006; Sun et al. 2012), and "weak turbulence regime" (Sun et al. 2012) were not observed in our cases. Although a longer-term dataset is needed to determine the frequency of such events, urban nocturnal heat sources likely produce a more frequent near-neutral (or slightly convective) NBL and hence a lower frequency of a more stable NBL, compared to natural landscapes. The first summer SURF-2015 experiment was a pre-experiment for testing deployed instruments, and results will be highly useful for planning and implementing such a series of experiments in the future.

Acknowledgements This work was supported by grants from National Key Projects of Ministry of Science and Technology of China (JFYS2016ZY01002213, 2014AA06A512, and 2015DFA20870), the Beijing Municipal Science and Technology Commission (Z151100002115045), and National Natural Science Foundation of China (41175015). We also acknowledge the support from the USDA-NIFA Agriculture and Food Research Initiative (awards 2015-67003-23460 and 2015-67003-23508). We are grateful to two anonymous reviewers for their careful review and valuable comments.

References

Al-Jiboori MH (2008) Correlation coefficients in urban turbulence. Boundary-Layer Meteorol 126(2):311–323

Andreas EL, Claffy KJ, Makshtas AP (2000) Low-level atmospheric jets and inversions over the western Weddell Sea. Boundary-Layer Meteorol 97(3):459–486
Angevine WM (2005) An integrated turbulence scheme for boundary layers with shallow cumulus applied to pollutant transport. J Appl Meteorol 44(9):1436–1452
Baker WE, Emmitt GD, Robertson F, Atlas RM, Molinari JE, Bowdle DA, Paegle J, Hardesty RM, Post MJ, Menzies RT, Krishnamurti TN, Brown RA, Anderson JR, Lorenc AC, McElroy J (1995) Lidar-measured winds from space: a key component for weather and climate prediction. Bull Am Meteorol Soc 76:869–888
Banta RM, Pichugina YL, Newsom RK (2003) Relationship between low-level jet properties and turbulence kinetic energy in the nocturnal stable boundary layer. J Atmos Sci 60(20):2549–2555
Banta RM, Pichugina YL, Brewer WA (2006) Turbulent velocity-variance profiles in the stable boundary layer generated by a nocturnal low-level jet. J Atmos Sci 63(11):2700–2719
Barlage M, Miao S, Chen F (2016) Impact of physics parameterizations on high-resolution weather prediction over two Chinese megacities. J Geophys Res Atmos 121(9):4487–4498
Barlow JF, Dunbar T, Nemitz E, Wood CR, Gallagher M, Davies F, O'Connor E, Harrison R (2011) Boundary layer dynamics over London, UK, as observed using Doppler lidar during REPARTEE-II. Atmos Chem Phys 11(5):2111–2125
Baumgarten G (2010) Twin Doppler Rayleigh/Mie/Raman lidar for wind and temperature measurements in the middle atmosphere up to 80 km. Atmos Meas Tech 3(6):1509–1518
Beyrich F (1997) Mixing height estimation from sodar data—a critical discussion. Atmos Environ 31(23):3941–3953
Caughey S, Wyngaard J, Kaimal J (1979) Turbulence in the evolving stable boundary layer. J Atmos Sci 36(6):1041–1052
Chanin M, Garnier A, Hauchecorne A, Porteneuve J (1989) A Doppler lidar for measuring winds in the middle atmosphere. Geophys Res Lett 16(11):1273–1276
Cohn SA, Angevine WM (2000) Boundary layer height and entrainment zone thickness measured by lidars and wind-profiling radars. J Appl Meteorol 39(8):1233–1247
Davies F, Middleton D, Bozier K (2007) Urban air pollution modelling and measurements of boundary layer height. Atmos Environ 41(19):4040–4049
Devara P (1989) Active remote-sensing of the atmosphere using lasers. J Sci Ind Res 48(2):71–83
Devara PCS, Jaya Rao Y, Sonbawne SM, Manoj MG, Dani KK, Saha SK (2015) First results of compact coherent Doppler wind lidar and its validation at IITM, Pune. India. Meteorol Appl 22(2):156–164
Emeis S, Schäfer K, Münkel C (2008) Surface-based remote sensing of the mixing-layer height-a review. Met Zeit 17(5):621–630
Emeis S, Münkel C, Vogt S, Müller WJ, Schäfer K (2004) Atmospheric boundary-layer structure from simultaneous SODAR, RASS, and ceilometer measurements. Atmos Environ 38(2):273–286
Flamant C, Pelon J, Flamant PH, Durand P (1997) Lidar determination of the entrainment zone thickness at the top of the unstable marine atmospheric boundary layer. Boundary-Layer Meteorol 83(2):247–284
Frehlich R, Hannon SM, Henderson SW (1994) Performance of a 2-um coherent Doppler lidar for wind measurements. J Atmos Ocean Technol 11(6):1517–1528
Grimmond CSB (2006) Progress in measuring and observing the urban atmosphere. Theor Appl Climatol 84(1–3):3–22
Haman CL, Lefer B, Morris GA (2012) Seasonal variability in the diurnal evolution of the boundary layer in a near-coastal urban environment. J Atmos Ocean Technol 29(5):697–710
He Q, Mao J, Chen J, Hu Y (2006) Observational and modeling studies of urban atmospheric boundary-layer height and its evolution mechanisms. Atmos Environ 40(6):1064–1077
Hong SY, Noh Y, Dudhia J (2006) A new vertical diffusion package with an explicit treatment of entrainment processes. Mon Weather Rev 134(9):2318–2341
Hu F, Li X, Chen H, Liu G (1999) Turbulence characteristics in the rough urban canopy layer. Clim Environ Res 4(3):252–258 **(in Chinese with English abstract)**
Jiang X, Wiedinmyer C, Chen F, Yang ZL, Lo JCF (2008) Predicted impacts of climate and land use change on surface ozone in the Houston, Texas, area. J Geophys Res Atmos 113:D20
Kaganov EI, Yaglom AM (1976) Errors in wind-speed measurements by rotation anemometers. Boundary-Layer Meteorol 10(1):15–34
Kosovic B, Curry JA (2000) A large eddy simulation study of a quasi-steady, stably stratified atmospheric boundary layer. J Atmos Sci 57(8):1052–1068
LeMone MA, Ikeda K, Grossman RL, Rotach MW (2003) Horizontal variability of 2-m temperature at night during CASES-97. J Atmos Sci 60(20):2431–2449
LeMone MA, Tewari M, Chen F, Dudhia J (2013) Objectively determined fair-weather CBL depths in the ARW-WRF model and their comparison to CASES-97 observations. Mon Weather Rev 141(1):30–54

LeMone MA, Tewari M, Chen F, Dudhia J (2014) Objectively determined fair-weather NBL features in ARW-WRF and their comparison to CASES-97 observations. Mon Weather Rev 142(8):2709–2732

Lenschow DH, Li XS, Zhu CJ, Stankov BB (1988) The stably stratified boundary layer over the Great Plains. Boundary-Layer Meteorol 42(1–2):95–121

Li J, Dou J (2014) Progress in urban meteorological experiments in Beijing. Adv Meteorol Sci Technol 1:38–47 **(in Chinese with English abstract)**

Liu G, Sun J, Jiang W, Liu H, Yuan R, Luo T (2009) Comprehensive observation research on urban atmospheric boundary layer—description of field experiment and analysis of micrometeorological properties in the surface layer. J Univ Sci Technol China 39(1):23–32 **(in Chinese with English abstract)**

Miao S, Chen F, Li Q, Fan S (2011) Impacts of urban processes and urbanization on summer precipitation: a case study of heavy rainfall in Beijing on 1 August 2006. J Appl Meteorol Climatol 50(4):806–825

Miao S, Dou J, Chen F, Li J, Li A (2012) Analysis of observations on the urban surface energy balance in Beijing. Sci China Earth Sci 55(11):1881–1890

Oke TR (2002) Boundary layer climates. Routledge, London, 435 pp

Pearson G, Davies F, Collier C (2010) Remote sensing of the tropical rain forest boundary layer using pulsed Doppler lidar. Atmos Chem Phys 10(13):5891–5901

Pichugina YL, Banta RM (2010) Stable boundary layer depth from high-resolution measurements of the mean wind profile. J Appl Meteorol Climatol 49(1):20–35

Pleim JE (2007) A combined local and nonlocal closure model for the atmospheric boundary layer. part I: model description and testing. J Appl Meteorol and Climatol 46(9):1383–1395

Pleim JE (2007) A combined local and nonlocal closure model for the atmospheric boundary layer. part II: application and evaluation in a mesoscale meteorological model. J Appl Meteorol Climatol 46(9):1396–1409

Rhodes ME, Lundquist JK (2013) The effect of wind-turbine wakes on summertime US Midwest atmospheric wind profiles as observed with ground-based doppler lidar. Boundary-Layer Meteorol 149(1):85–103

Roth M (2000) Review of atmospheric turbulence over cities. Q J R Meteorol Soc 126(564):941–990

Singh UN, Kavaya MJ (2004) Overview and accomplishments of NASA's Laser Risk Reduction Program at NASA Langley Research Center, 22nd Internation laser radar conference (ILRC), 12–16 July 2004. Matera, Italy

Sathe A, Mann J, Gottschall J, Courtney MS (2011) Can wind lidars measure turbulence? J Atmos Ocean Technol 28(7):853–868

Stull RB (1988) An introduction to boundary layer meteorology. Springer Science & Business Media, New York, 670 pp

Sun J, Mahrt L, Banta RM, Pichugina YL (2012) Turbulence regimes and turbulence intermittency in the stable boundary layer during CASES-99. J Atmos Sci 69(1):338–351

Tucker SC, Senff CJ, Weickmann AM, Brewer WA, Banta RM, Sandberg SP, Law DC, Hardesty RM (2009) Doppler lidar estimation of mixing height using turbulence, shear, and aerosol profiles. J Atmos Ocean Technol 26(4):673–688

Vickers D, Mahrt L (2004) Evaluating formulations of stable boundary layer height. J Appl Meteorol 43(11):1736–1749

Westwater E, Han Y, Irisov V, Leuskiy V, Kadygrov E, Viazankin S (1999) Remote sensing of boundary layer temperature profiles by a scanning 5-mm microwave radiometer and RASS: comparison experiments. J Atmos Ocean Technol 16(7):805–818

Wilczak JM, Oncley SP, Stage SA (2001) Sonic anemometer tilt correction algorithms. Boundary-Layer Meteorol 99(1):127–150

Zhong S, In H, Clements C (2007) Impact of turbulence, land surface, and radiation parameterizations on simulated boundary layer properties in a coastal environment. J Geophys Res Atmos 112:D13